Instability and sensitivity of the flow inside a radial compressor vaneless diffuser

Andrea Ferraro & Giovanni Beati

March 9, 2017

Abstract

This project deals with a modal stabilty analysis of a flow inside a vaneless radial compressor diffuser. The numerical analysis has been performed using the program $pastaAxi3d$, developed at Politecnico di Milano under the supervision of Franco Auteri. The analysed geometry is axisymmetric and the inlet velocity profiles of the basic flow have been taken, for different operating conditions, from solutions obtained by solving the Reynolds-averaged Navier-Stokes equations. For all operating conditions, the stationary base flow, left and right eigenvectors and corresponding eigenvalues have been computed. In particular, solutions have been obtained for different values of the azimuthal wave number. It was found that unstable solutions are obtained above a certain value of the azimuthal wave number. Moreover, a structural sensitivity analysis has been performed for all unstable eigenvalues found.

1 Introduction

The performance of compressors at low mass-flows is characterized by the occurrence of unsteady flow phenomena surge and rotating stall. These instabilities can cause noise and critical operating conditions with strong dynamical loading on the blades. Therefore, they cannot be tolerated during compressor operation. To avoid these phenomena, compressors are operated at higher mass-flow rates than those prevailing at the critical operating conditions to keep a safety margin to the stability limit. Limiting of the compressor operating range results in the loss of high-pressure ratios, which makes this issue an interesting subject to research (S. Ljevar (2006)). Figure (1) shows the complete geometry of the compressor and the shaded section represents the axisymmetric portion of the diffuser domain for this analysis.
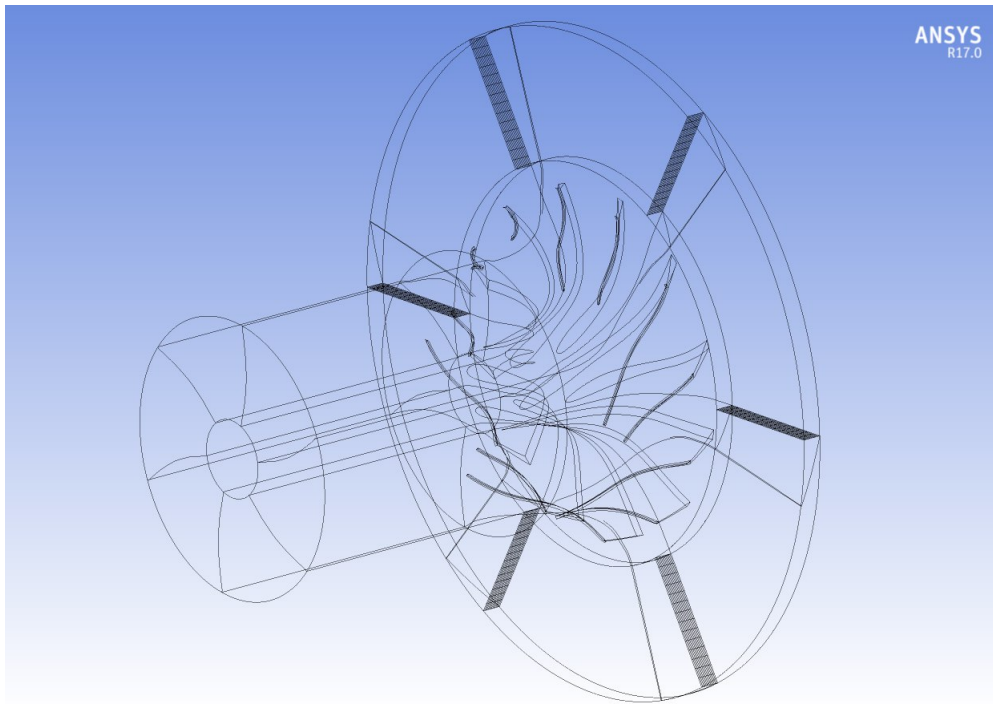
Figure 1: Complete geometry of the compressor with the impeller and the diffuser. The shaded area represents the axisymmetric section of the diffuser taken as computational domain for this analysis.

2   PastaAxi3d

$pastaAxi3d$ is a program for linear and nonlinear stability analysis written in Fortran90 (Auteri (2016)). The program is able to compute the steady base flow, direct and adjoint eigenvectors with the corresponding eigenvalues and the structural sensitivity function. Two compulsory input files are always necessary, irrespective of the kind of analysis that must be carried out. These files are called program_data.in and problem_data.in. The program_data.in file controls the execution of the program: in this file the requested analysis and the necessary parameters are specified. In the first section of this file it is possible to choose the analysis type: in this work it has been used the steady state computation, the eigenvalue computation and structural sensitivity computation. The file problem_data.in contains the control parameters, such as the Reynolds number and the azimuthal wave number, for the flow under investigation, the boundary conditions and the forcing specification.

3   Problem formulation

The governing equations of the problem are presented in this section.

3.1 Navier-Stokes equations

The fluid motion is described by the two-dimensional unsteady incompressible Navier-Stokes equations

$$\begin{cases} \frac{\partial \mathbf{u}}{\partial t} + (\mathbf{u} \cdot \nabla)\mathbf{u} - \frac{1}{Re}\nabla^2\mathbf{u} + \nabla p = 0 \\ \nabla \cdot \mathbf{u} = 0 \end{cases} \tag{1}$$

where $\mathbf{u} = \mathbf{u}(u_x, u_r, u_\theta, t)$. The equations are made dimensionless by choosing a characteristic length scale X^* that is the width of the channel under investigation and a reference velocity $U^* = \sqrt{u_{r,max}^2 + u_{\theta,max}^2}$, depending on inlet profile velocity which allow to define the Reynolds number, $Re = \frac{U^*X^*}{\nu}$.

3.2 Linearized equations

The starting point of the linear stability analysis is the linearization of the Navier−Stokes equations. The velocity and pressure fields are then considered as the linear combination of two fields, $\mathbf{u} = \mathbf{U} + \mathbf{u}'$ and $p = P + p'$ which, substituted into the Navier-Stokes equations, lead to the base flow and the perturbed systems.

3.2.1 Base Flow

$$\begin{cases} (\mathbf{U} \cdot \nabla)\mathbf{U} - \frac{1}{Re}\nabla^2\mathbf{U} + \nabla P = 0 \\ \nabla \cdot \mathbf{U} = 0 \end{cases} \tag{2}$$

The boundary conditions are specified in the program_data.in file. Each row corresponds to a side of the domain that is an axialsimmetric channel with a height to width ratio equal to 6.794. The first three columns correspond to the three components of the velocity field while the others represent the no-stress conditions.

```
"
.t.  .t.  .t.  .f.  .f.  'w' # 1
.f.  .f.  .f.  .t.  .t.  'o' # 2   OUTFLOW
.t.  .t.  .t.  .f.  .f.  'w' # 3
.t.  .t.  .t.  .f.  .f.  'i' # 4   IN
#
0.    0.  0.  0.  0.    0.  0.  0.  0.  0.    0.  0.  0.  0.  0.      # 1
0.    0.  0.  0.  0.    0.  0.  0.  0.  0.    0.  0.  0.  0.  0.      # 2 OUTFLOW
0.    0.  0.  0.  0.    0.  0.  0.  0.  0.    0.  0.  0.  0.  0.      # 3
313. 1.  0.  0.  0.    0.  1.  0.  0.  0.    0.  1.  0.  0.  0.      # 4 IN
#
0 0 #_ volume forcing f_z
0 0 #_ volume forcing f_r
0 0 #_ volume forcing f_theta
```

Figure 2: Boundary conditions inside the program_data.in file

3.2.2 Disturbance equations

After dropping non linear terms, the Navier-Stokes equations for the perturbations are:

$$\begin{cases} \frac{\partial \mathbf{u}'}{\partial t} + (\mathbf{U} \cdot \nabla)\mathbf{u}' + (\mathbf{u}' \cdot \nabla)\mathbf{U} - \frac{1}{Re}\nabla^2\mathbf{u}' + \nabla p' = 0 \\ \nabla \cdot \mathbf{u}' = 0 \end{cases} \tag{3}$$

3

The adjoint linearized NavierStokes system of equations is obtained from the direct one by multiplying it by two test functions, $\mathbf{v}'$ and q', and integrating by parts. After standard mathematical manipulation, the adjoint linearized Navier-Stokes equations become Canton (2012-2013):

$$\begin{cases} \frac{\partial \mathbf{v}'}{\partial t} + (\mathbf{U} \cdot \nabla)\mathbf{v}' - (\nabla U) \cdot \mathbf{v}' + \frac{1}{Re}\nabla^2 \mathbf{v}' + \nabla q' = 0 \\ \nabla \cdot \mathbf{v}' = 0 \end{cases} \tag{4}$$

3.2.3 Modal Stability

The objective of this analysis is to describe the instability, the shape of the unstable modes and to find out where the instability mechanism is located in the flow field. Once the base flow has been computed, the second step consists in the solution of the linearized problem; under the assumption of normal modes, the velocity and pressure perturbations can be written as $\mathbf{u}'(x, r, \theta, t) = e^{(\lambda t + \beta \theta)}\hat{\mathbf{u}}(x, r)$, $p'(x, r, \theta, t) = e^{(\lambda t + \beta \theta)}\hat{p}(x, r)$; the direct linearized Navier-Stokes equations result in the following generalized eigenvalue problem in the unknowns $\lambda_j = \lambda_{r,j} + i\lambda_{i,j}$ ($\lambda_{i,j}$ representing the frequency and $\lambda_{r,j}$ the amplification/damping rate of the perturbation), $\hat{\mathbf{u}}_j$ and $\hat{p}_j$:

$$\begin{cases} \lambda_j \hat{\mathbf{u}}_j + (\mathbf{U} \cdot \nabla)\hat{\mathbf{u}}_j + (\hat{\mathbf{u}}_j \cdot \nabla)\mathbf{U} - \frac{1}{Re}\nabla^2 \hat{\mathbf{u}}_j + \nabla \hat{p}_j = 0 \\ \nabla \cdot \hat{\mathbf{u}}_j = 0 \end{cases} \tag{5}$$

where λ_j is the eigenvalue and $\hat{\mathbf{u}}$ and $\hat{p}$ are the eigenfunctions of the direct problem. To perform the structural sensitivity analysis, the adjoint eigenfunctions are also needed, therefore the adjoint eigenvalue problem is introduced here. Starting from the adjoint linearized NavierStokes equations, and repeating the same steps used for the direct one, the corresponding eigenvalue problem is easily obtained:

$$\begin{cases} -\lambda_j \hat{\mathbf{v}}_j + (\mathbf{U} \cdot \nabla)\hat{\mathbf{v}}_j - (\nabla U) \cdot \hat{\mathbf{v}}_j + \frac{1}{Re}\nabla^2 \hat{\mathbf{v}}_j + \nabla \hat{q}_j = 0 \\ \nabla \cdot \hat{\mathbf{v}}_j = 0 \end{cases} \tag{6}$$

where λ_j is the eigenvalue and $\hat{\mathbf{v}}$ and $\hat{q}$ are the eigenfuctions of the adjoint problem.

3.2.4 Structural Sensitivity

The region where the instability mechanism acts cannot be identified from the study of the direct and adjoint eigenfunctions separately. This is because, in general, there is a large difference in the spatial structure of the direct and adjoint modes. The aim of this analysis is to investigate in what region of the flow field the wavemaker is located, more precisely, where in space a modification in the structure of the problem, represented by a localized velocity feedback, is able to produce the greatest drift of the least stable eigenvalue. This, indeed, is the core of the instability mechanism. After a few manipulations (as described in Canton (2012-2013)) and thanks to the adjoint eigenvalue problem, the conclusion is that the linearized

system is most sensitive to perturbations represented by a spatially localized feed-back located in the maximum of the function:

$$s(x,r) = \frac{||\mathbf{v}(\hat{\mathbf{x}}, \mathbf{r})_i|| \quad ||\mathbf{u}(\hat{\mathbf{x}}, \mathbf{r})_i||}{|\int_\Omega \hat{\mathbf{v}}_i \cdot \hat{\mathbf{u}}_i|} \tag{7}$$

here referred to as *structural sensitivity parameter*.

4   Case analysis

The case of the vaneless diffuser is presented in this section and figure (3) shows the computational domain with dimensionless lengths. In the first step we produced a mesh with a high refinement level at the inlet patch that was able to resolve and capture the strong gradients of the inlet profiles. The aim of the mesh process was to have a good mesh and to keep the number of mesh elements limited according to our computational resource and in order to limit the simulation time; then the steady base flow was computed and the Reynolds number was gradually increased from $Re = 100$ with a small step up to $Re = 890$ for all the inlet profiles enabling the restart flag in the program_data.in that allows to restart the simulation from the previous one and facilitating the convergence of the numerical scheme. The upper limit of the Reynolds number was the maximum that has been reached after that the simulation diverges probably due to the lack of mesh's elements and the kind of discretization for diffusion and convective terms. Figure (4) shows the velocity magnitude for the different $Reynolds$ number computed. A diffusive behaviour for the flow at low $Reynolds$ number can be noted and the creation of a fluid core with diffusive contour as the $Reynolds$ number increases with the tendency to curve inside the channel. The contour of the core flow can be resolved with greater accuracy reducing the diffusivity at the boundaries by increasing the elements of the mesh with additional computational costs.
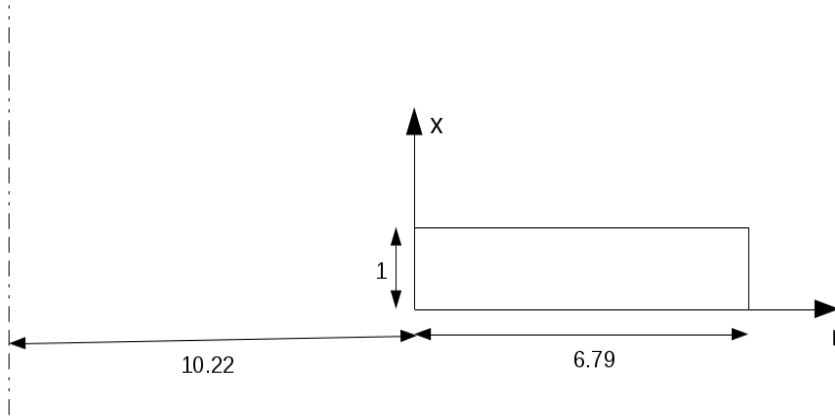
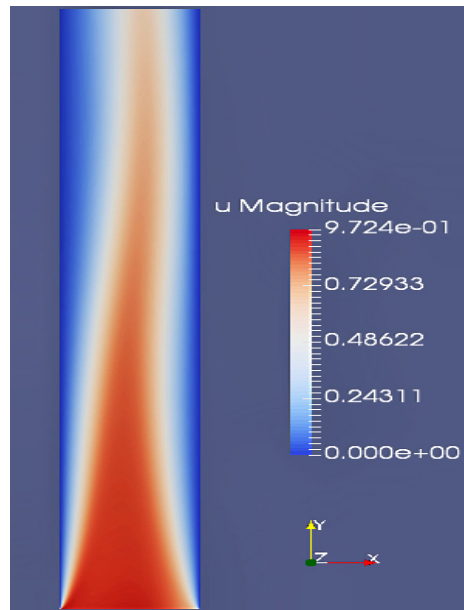Figure 3: Computational domain and nondimensional dimensions
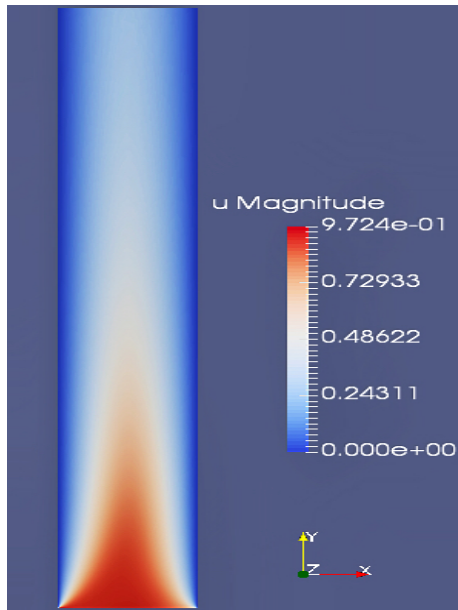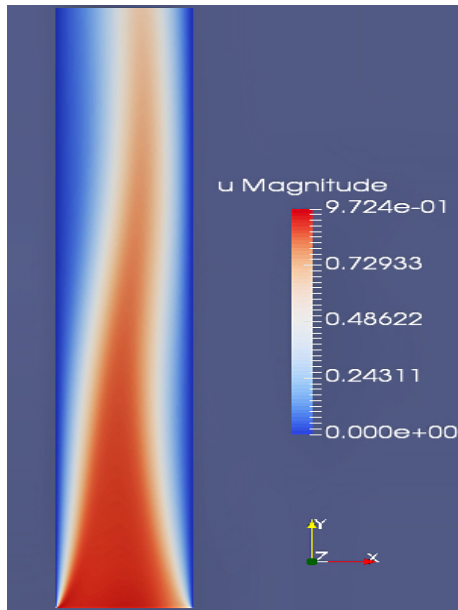
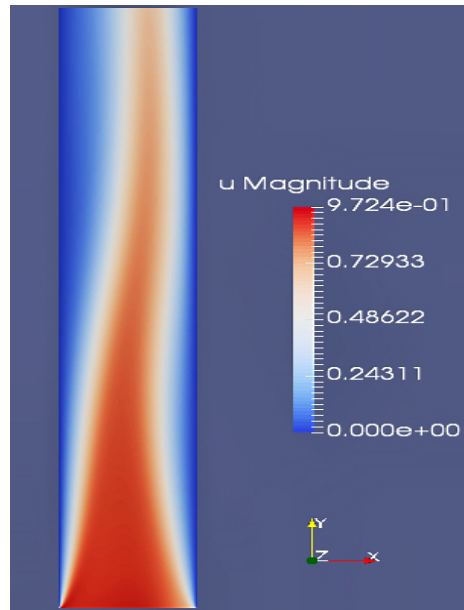(a) Steady base flow $Re = 100$
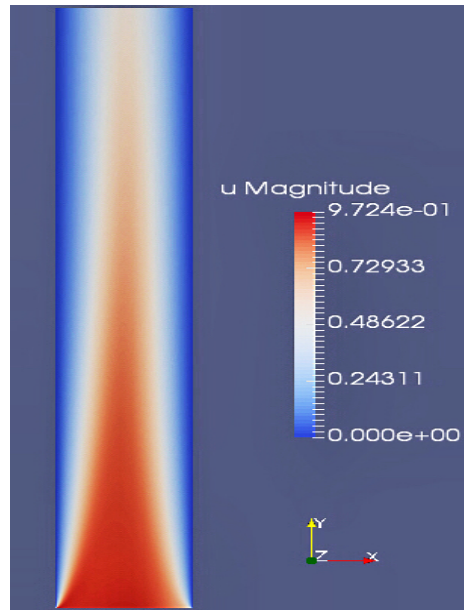
(b) Steady base flow $Re = 500$
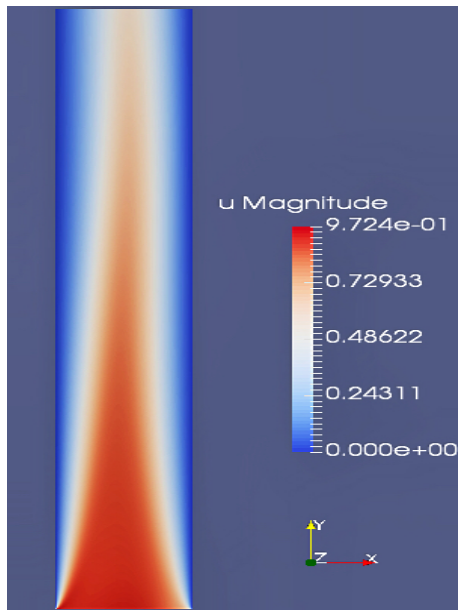
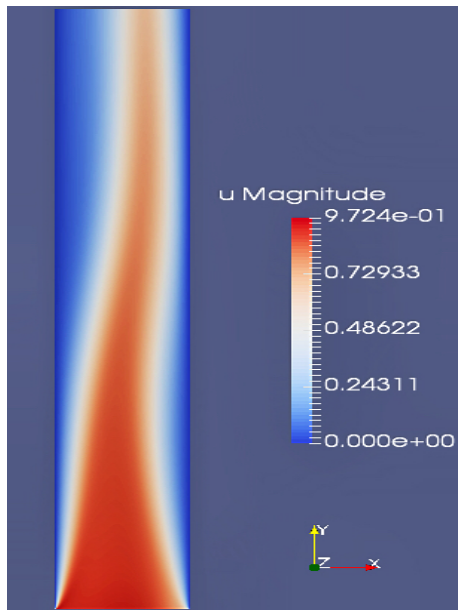(c) Steady base flow $Re = 600$

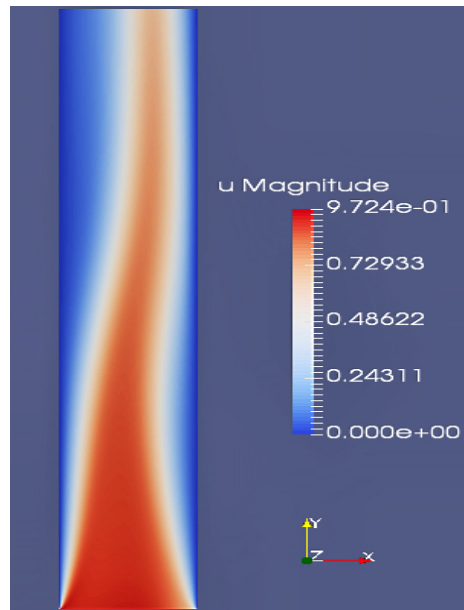(d) Steady base flow $Re = 700$

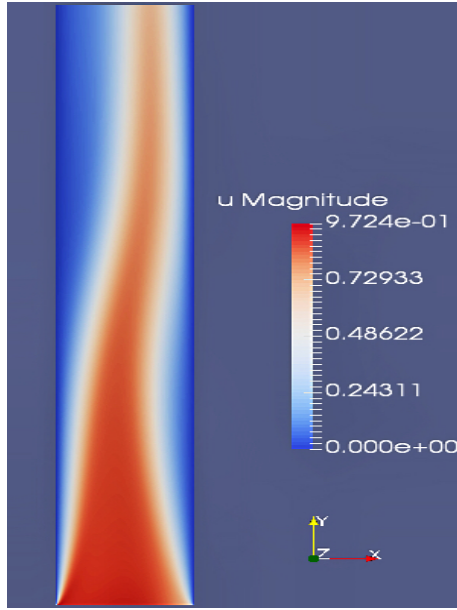(e) Steady base flow $Re = 750$

(f) Steady base flow $Re = 800$


(g) Steady base flow $Re = 850$


(h) Steady base flow $Re = 870$

(i) Steady base flow $Re = 890$

Figure 4: Magnitude of velocity for the steady base flow with Re varying from 100 up to 890

Different inlet profiles have been tested in order to take into account of the effect of the angle of attack in the subsequent stability analysis. The inlet profiles are presented in figure (5). All these profiles have been extracted at the outlet from a computation of an industrial centrifugal compressor with a RANS simulation with scalable wall function for the $k-\omega SST$ turbulence model. They are representative of different operating points of the radial compressor with the dimensionless mass flow rate varying from 0.66 up to 0.8 at $60700[rpm]$ (all the mass flow rates have been divided by a design operating condition). A summary of the different cases is found in table (1) and the inlet angle was defined from the radial direction as the $\alpha = atan\frac{\bar{u}_\theta}{\bar{u}_r}$ with $\bar{u}_r$ and $\bar{u}_\theta$ representing the mean of the radial and azimuthal inlet profiles. A better view of the fluid motion inside this channel can be performed with an analysis of the components of the velocity field as shown in figures (6), (7), (8). It should be underlined that the depth component takes on a vortex structure of low intensity, with a different behaviour in the case with the lowest mass flow with the formation of a vortex in the opposite direction from the other ones. The radial component also shows a small recirculation zone near to the right boundary that moves towards the inlet as the mass flow decreases.
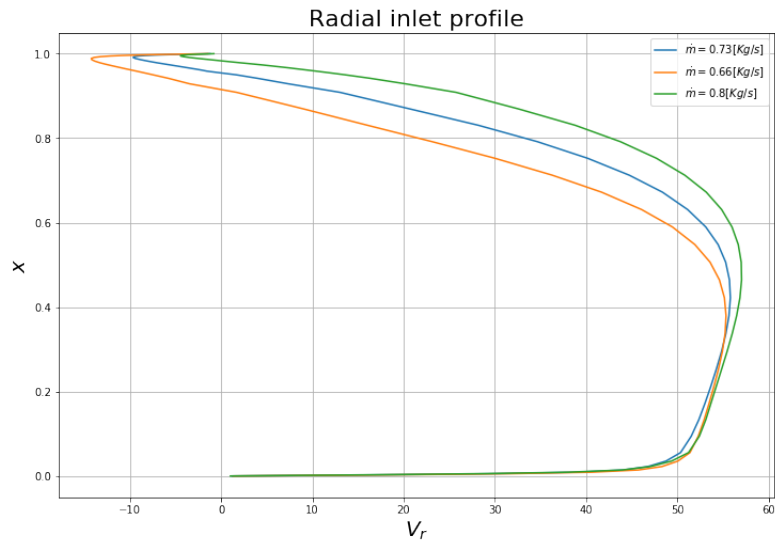
(a) Radial inlet profile
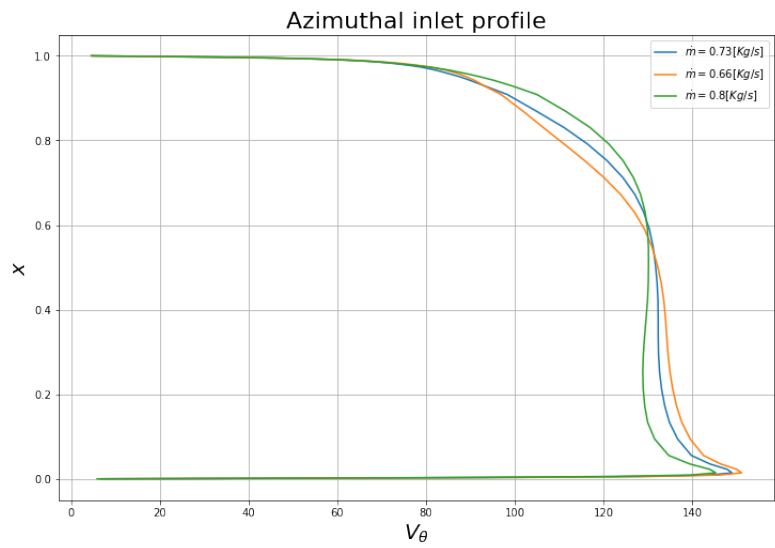
(b) Azimuthal inlet profile

Figure 5: Inlet velocity profiles

Table 1: Mass flux and angle of inlet velocity for the cases analyzed
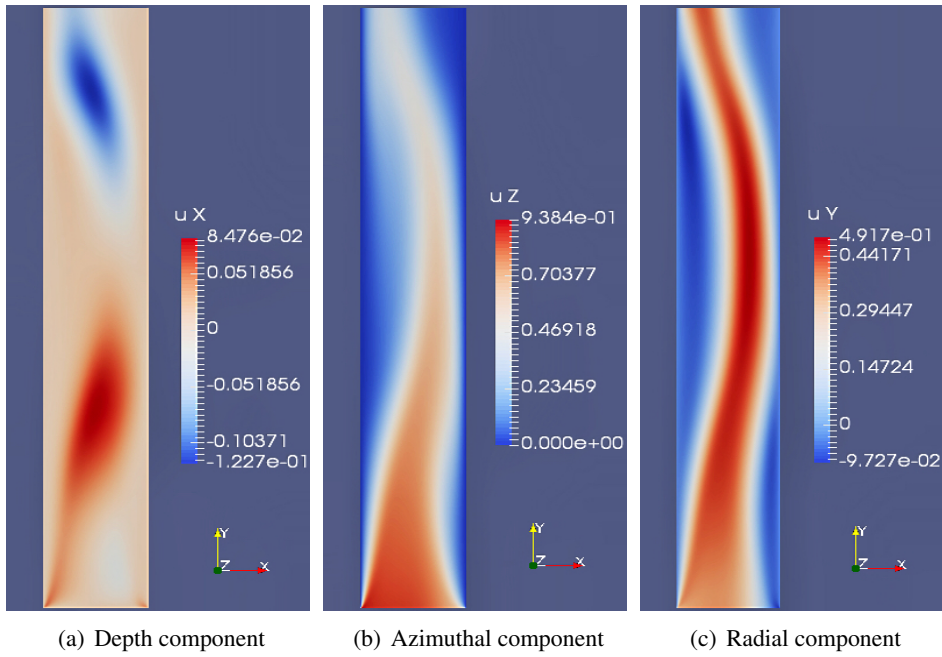
$\dot{m}/\dot{m}_{design}$	α
0.66	$83°$
0.73	$80°$
0.8	$76.5°$

(a) Depth component   (b) Azimuthal component   (c) Radial component

Figure 6: Velocity component for $\dot{m}/\dot{m}_{design} = 0.66$

(a) Depth component   (b) Azimuthal component   (c) Radial component
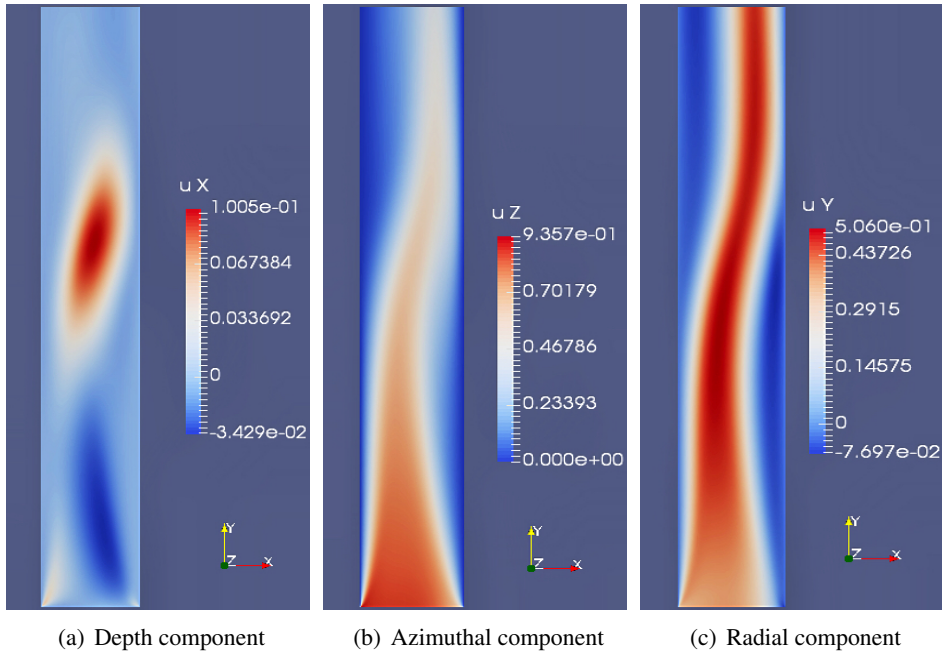
Figure 7: Velocity component for $\dot{m}/\dot{m}_{design} = 0.73$

(a) Depth component   (b) Azimuthal component   (c) Radial component
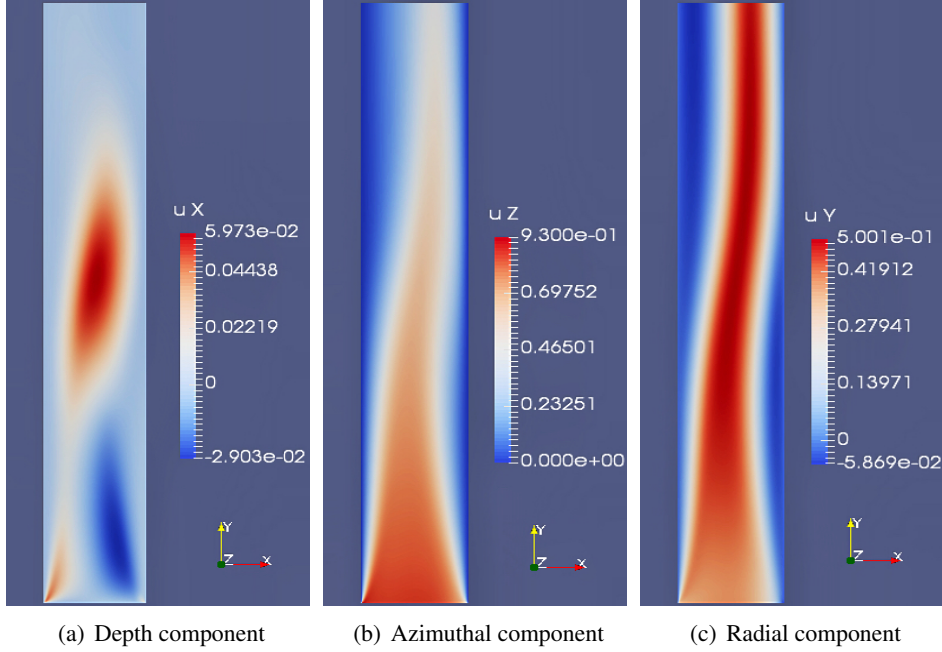
Figure 8: Velocity component for $\dot{m}/\dot{m}_{design} = 0.8$

5   Computing the spectrum

The global stability analyses of this turbulent flow is carried out based on the so called *mean-flow approach* as described by Sipp & Lebedev (2007). This approach simply relies on the linearization of the mass conservation and momentum equations around the given time-averaged mean flow. Here the base flow has not been computed with a turbulence model, but only the inlet profile came from a RANS computation. This is probably the biggest approximation in this work but this approach can also give a qualitative estimation of the leading frequency of large-scale organized waves as explained by Carini *et al.* (2016). Solving the generalized eigenvalue problem for λ described in eq. (5) it has been computed the spectrum and any solution $\hat{u}$ associated with an eigenvalue λ represents a global mode of the mean flow with a growth rate $Re(\lambda)$ and angular frequency $Im(\lambda)$. For this kind of analysis in $PASTA$ the user has to choose how many eigenvalues to compute in each run and the point in the complex plane around which they are evalueted. The output data are the eigenvalues and, possibly, some selected eigenvectors. In figures (9) and (10) there are two examples of spectra with all eigenvalues being stable (that means $Re(\lambda < 0)$) and at least one eigenvalue with real part > 0 respectively. Comparing the stable and unstable spectra it is clearly apparent the eigenvalue with the real part larger than zero and for all the cases two different branches that changes slope as the imaginary part increases.
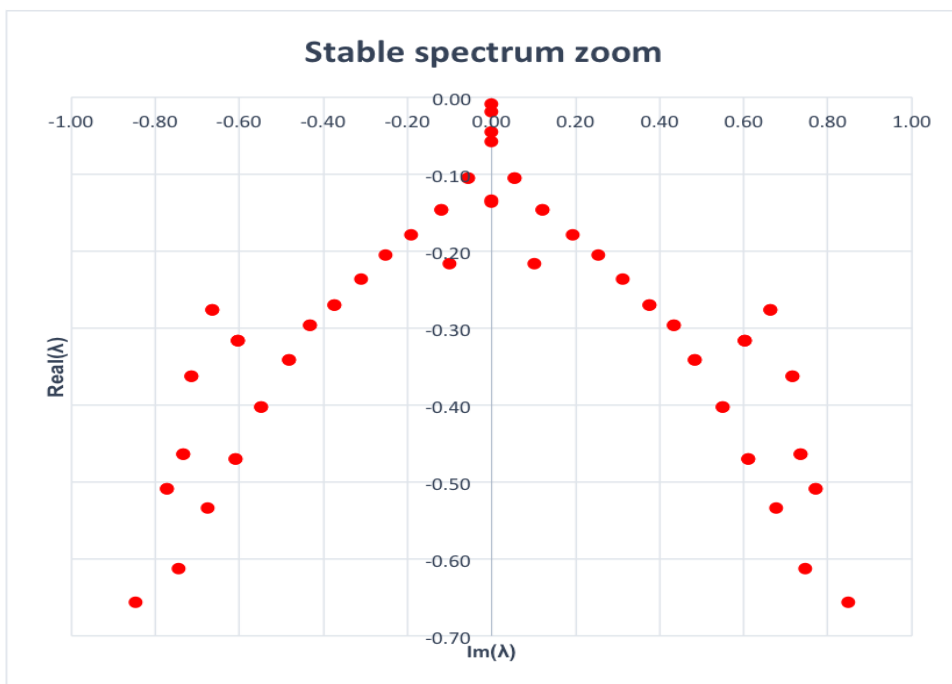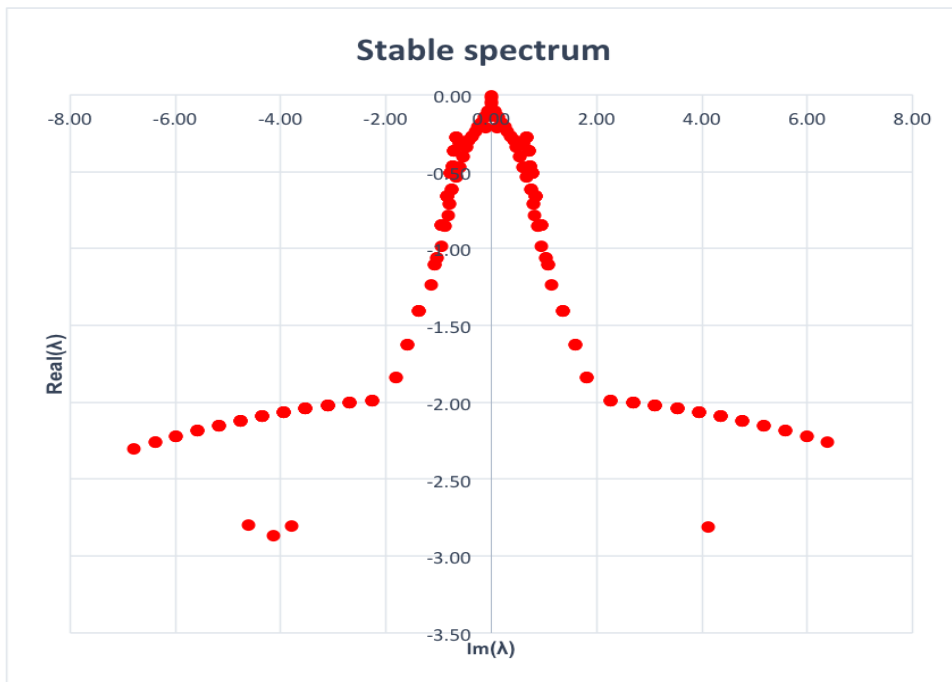
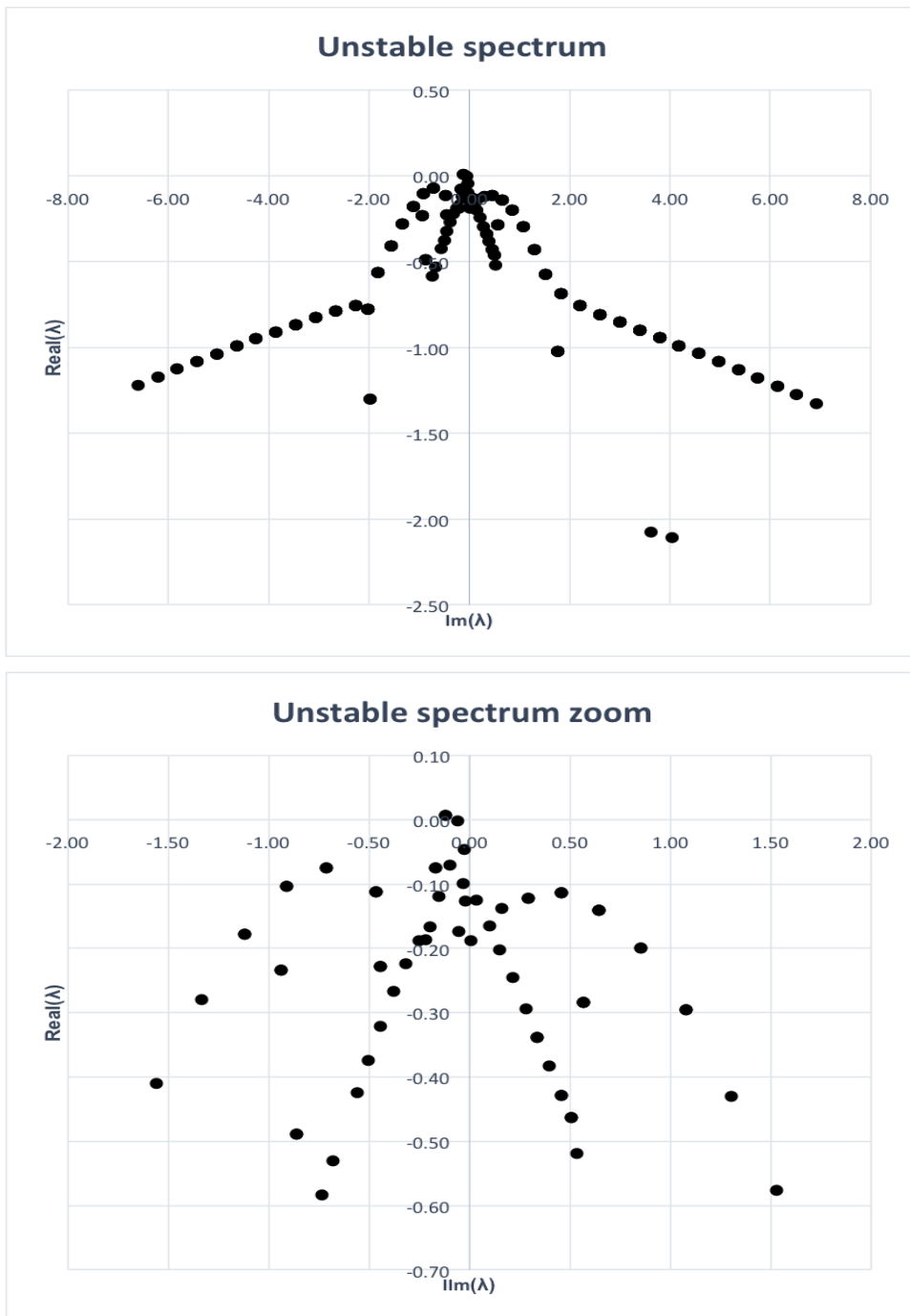Figure 9: Example of stable spectrum with a zoom near the immaginary axis

12

Figure 10: Example of unstable spectrum with a zoom near the immaginary axis

Figure 11 presents the variation of the growth rate and the circular frequency as a function of the wave number in the azimuthal direction. For all cases the flow

remains stable when the azimuthal wave number is zero or small. Increasing the wave number above a certain threshold the flow becomes unstable. This occurs here for values of $3 <= \beta <= 5$. Moreover, it is shown that all solutions are unstationary but the frequency remains low $O(10^{-2} - 10^{-3})$.
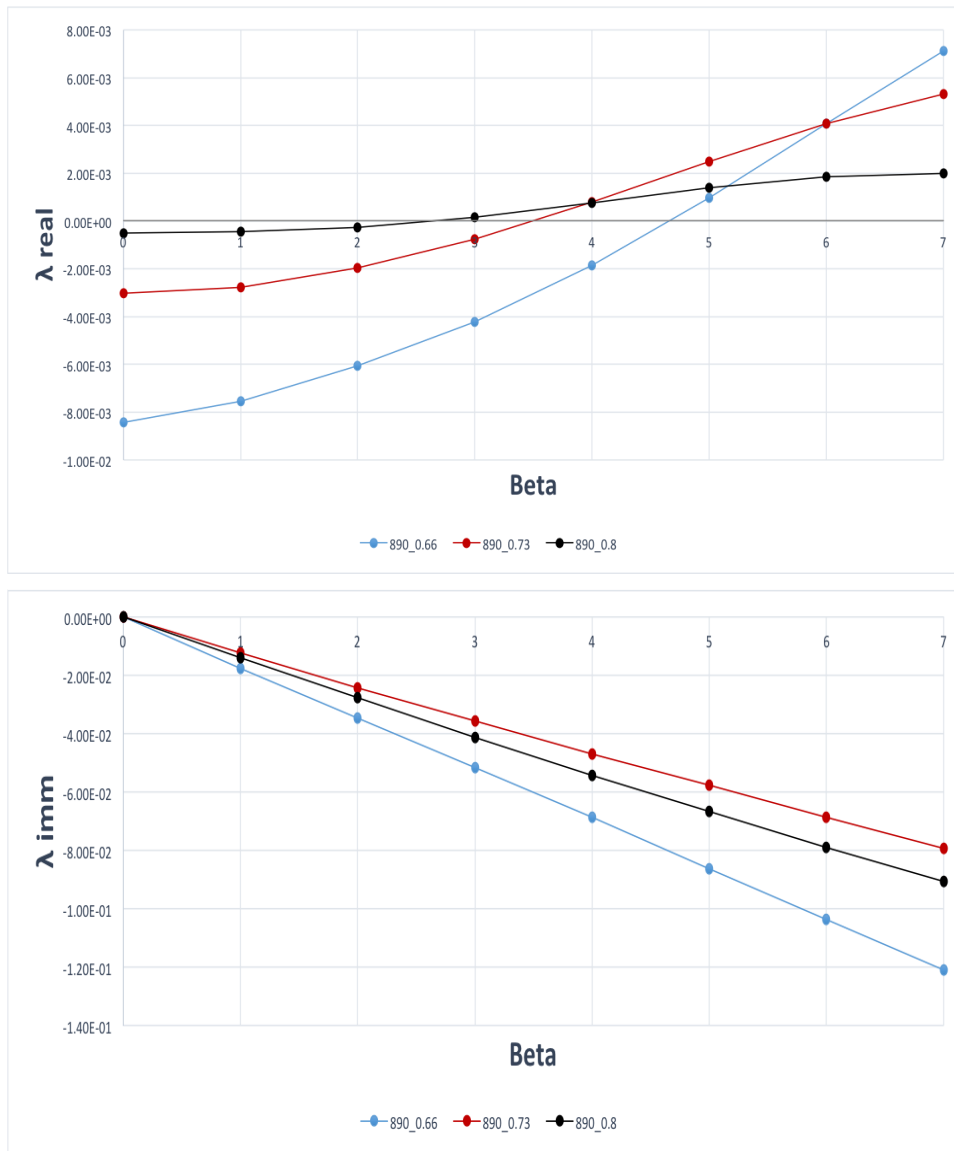
Figure 11: Real and imaginary part of the most unstable eigenvalue for different operating conditions at $Re = 890$

Usually it is interesting to plot the eigenvectors associated with the eigenvalues that are the nearest to the imaginary axis, but in some cases the user may want to investigate eigenvectors associated with other eigenvalues, to investigate their

physical significance/meaning. In figures 12-(23) only the most unstable direct eigenvectors are presented with different wave number in the azimuthal direction. Analysing the case with $\dot{m}/\dot{m}_{design} = 0.8$ in figures (12),(13),(14),(15) it is clearly apparent a $3D$ vortex shape in the middle of the channel and the depth component changes direction between $\beta = 4$ and $\beta = 5$. But for $\beta = 7$ there is a beginning of a double vortex that increases the fluid motion from the hub and shroud walls to the center of the channel. The successive figures (16), (17), (18), (19) are concerned with a test with a dimensionless mass flow rate of 0.73 and they shows a similar $3D$ vortex structure changing the rotation from clockwise to counterclockwise as the azimuthal wave number increases. The most interesting case is that one displayed in figures (20) (21) (22) (23) related to the lowest mass flow rate tested. Here the instabilty occurs for a high azimuthal wave number with a big vortex that sizes almost entirely the channel and changes its orientation twice from $\beta = 5$ to $\beta = 7$.
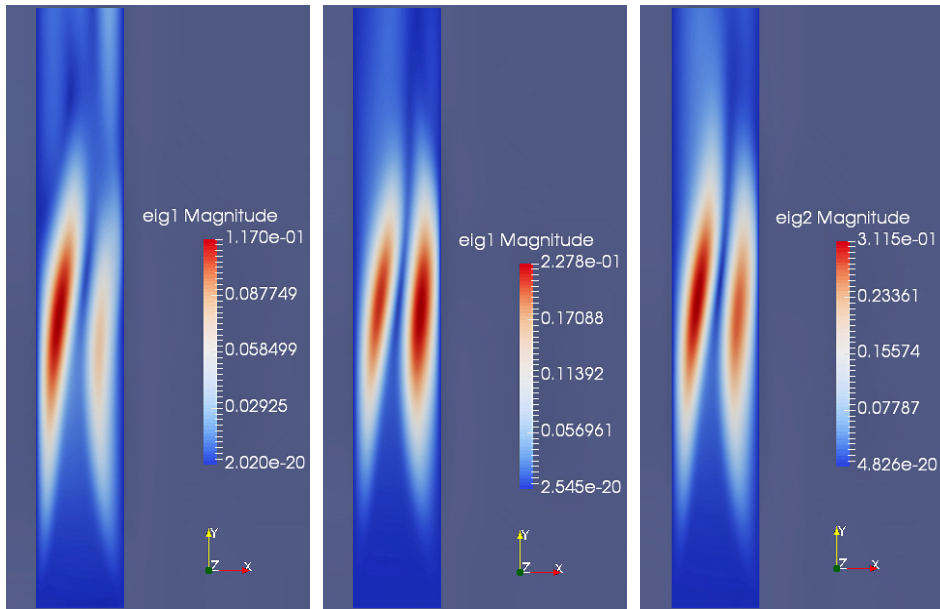
(a) Magnitude of perturbation velocity with $\beta = 3$

(b) Magnitude of perturbation velocity with $\beta = 4$

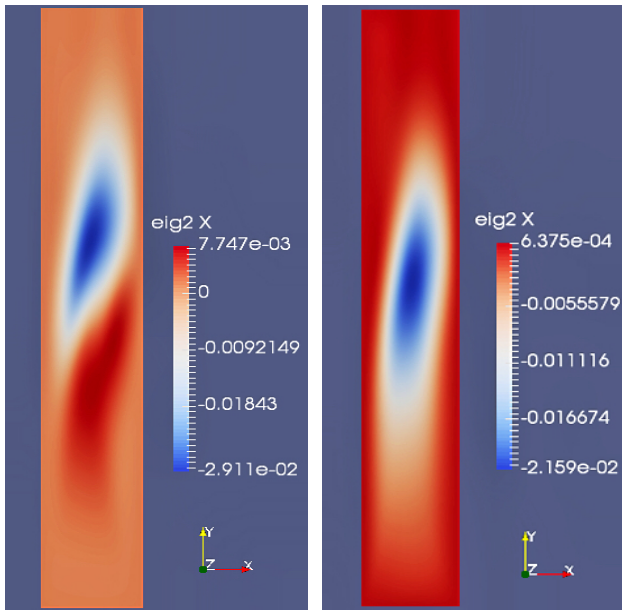(c) Magnitude of perturbation velocity with $\beta = 5$
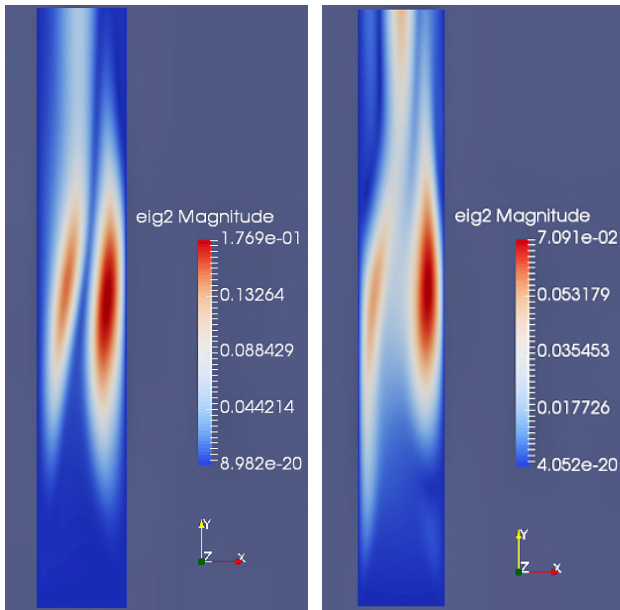
(d) Magnitude of perturbation velocity with $\beta = 6$

(e) Magnitude of perturbation velocity with $\beta = 7$

Figure 12: Magnitude of velocity for the most unstable modes with $\dot{m}/\dot{m}_{design} = 0.8$ and $Re = 890$
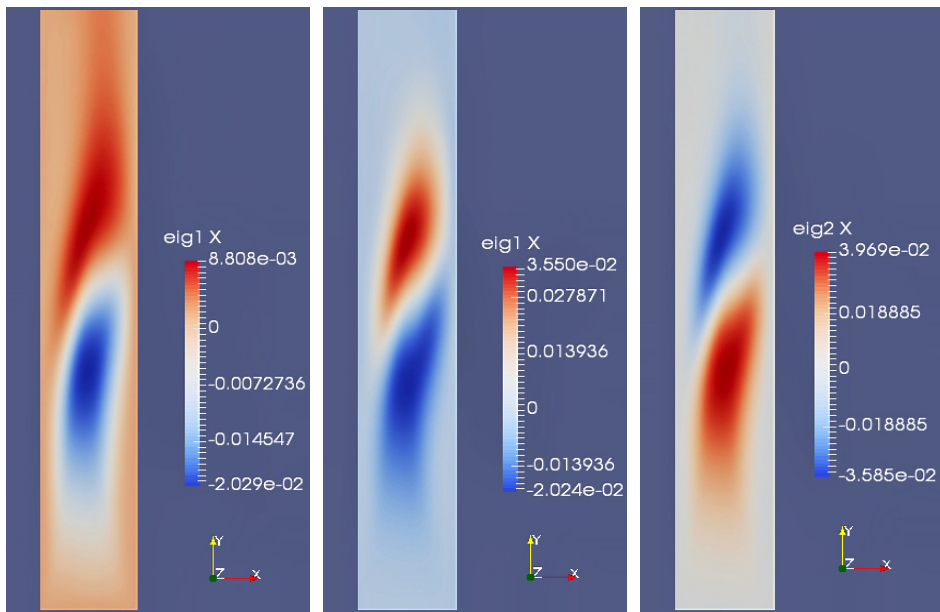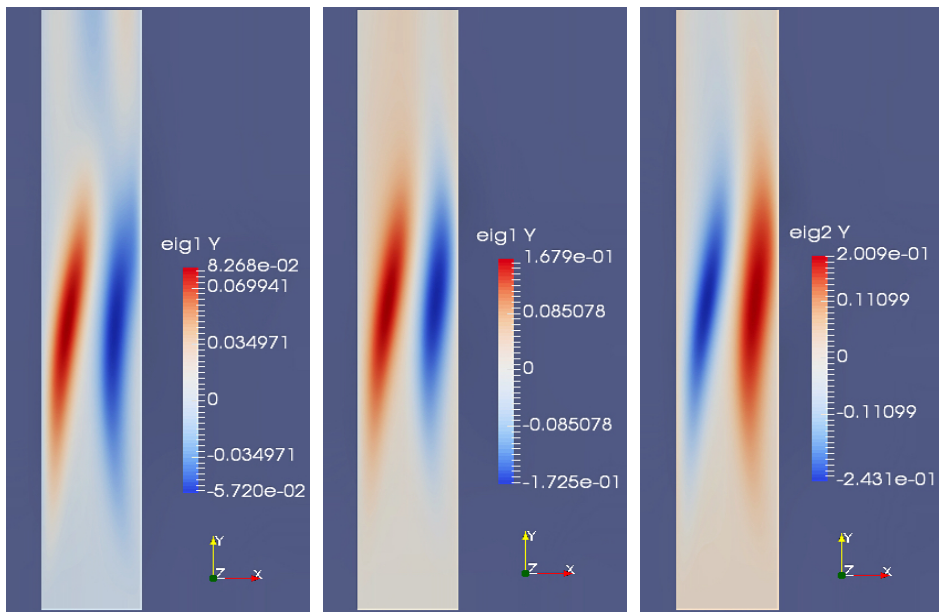

(a) Depth component of perturbation velocity with $\beta = 3$

(b) Depth component of perturbation velocity with $\beta = 4$

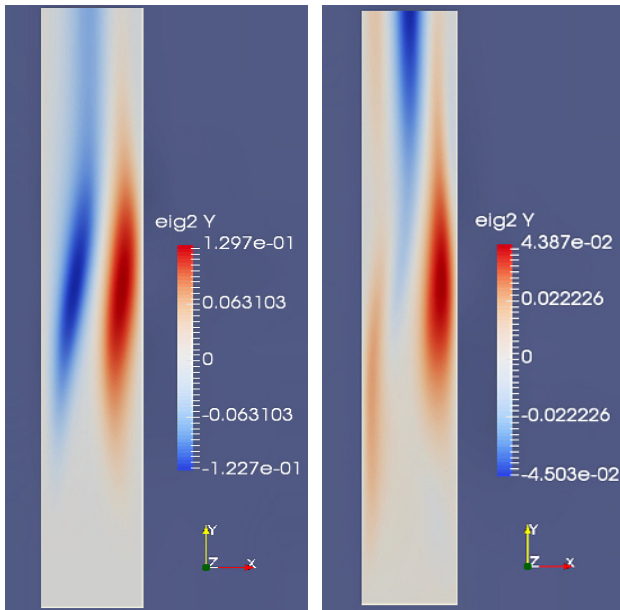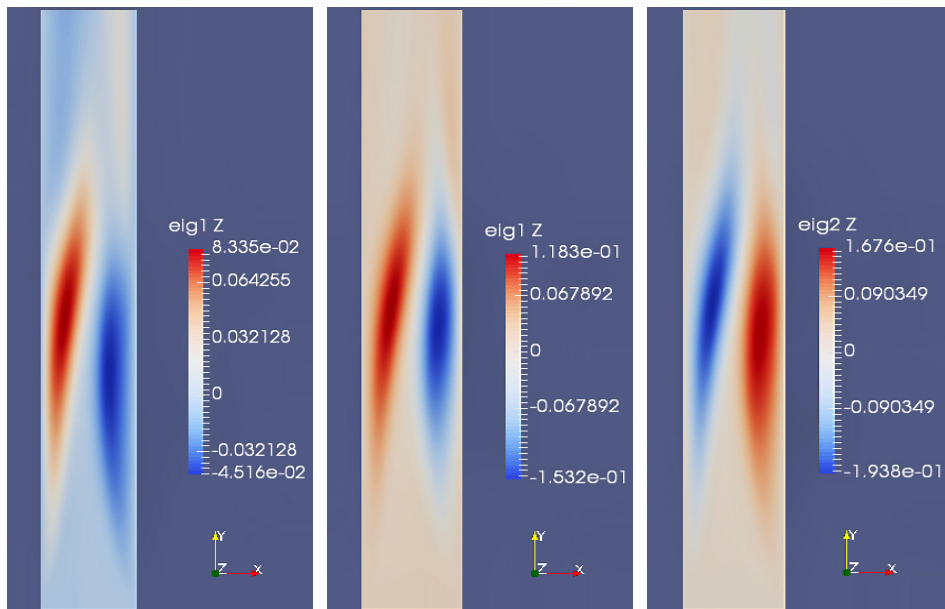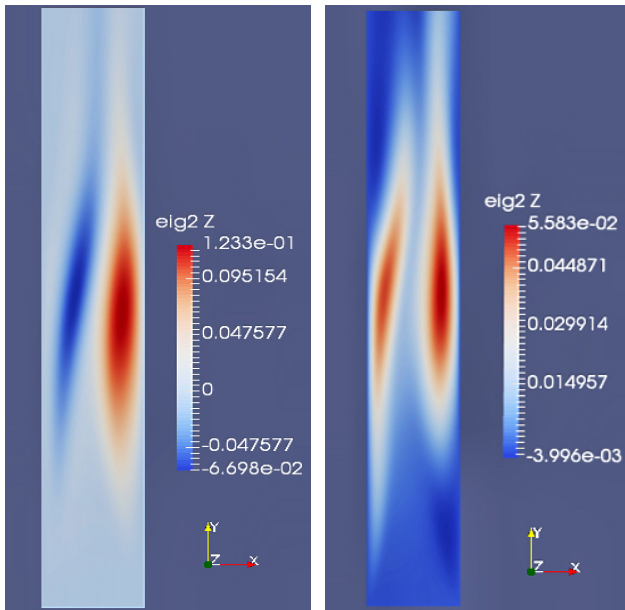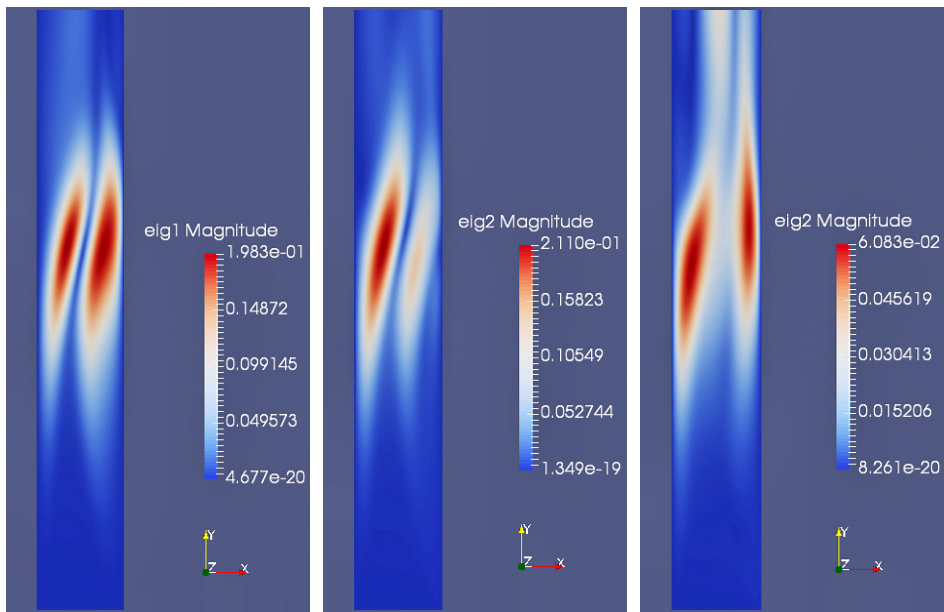(c) Depth component of perturbation velocity with $\beta = 5$

16

(d) Depth component of pertur-
bation velocity with $\beta = 6$

(e) Depth component of pertur-
bation velocity with $\beta = 7$

Figure 13: Depth component of perturbation velocity for the most instable modes
with $\dot{m}/\dot{m}_{design} = 0.8$ and $Re = 890$

(a) Radial component of pertur-
bation velocity with $\beta = 3$

(b) Radial component of pertur-
bation velocity with $\beta = 4$

(c) Radial component of pertur-
bation velocity with $\beta = 5$

(d) Radial component of pertur-
bation velocity with $\beta = 6$

(e) Radial component of pertur-
bation velocity with $\beta = 7$

Figure 14: Radial component of velocity for the most unstable modes with
$\dot{m}/\dot{m}_{design} = 0.8$ and $Re = 890$

(a) Azimuthal component of
perturbation velocity with $\beta = 3$

(b) Azimuthal component of
perturbation velocity with $\beta = 4$

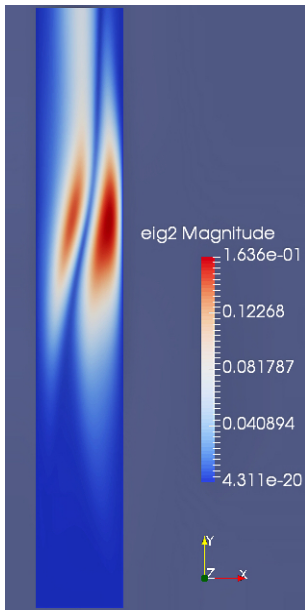(c) Azimuthal component of
perturbation velocity with $\beta = 5$

(d) Azimuthal component of perturbation velocity with $\beta = 6$ (e) Azimuthal component of perturbation velocity with $\beta = 7$

Figure 15: Azimuthal component of velocity for the most unstable modes with $\dot{m}/\dot{m}_{design} = 0.8$ and $Re = 890$
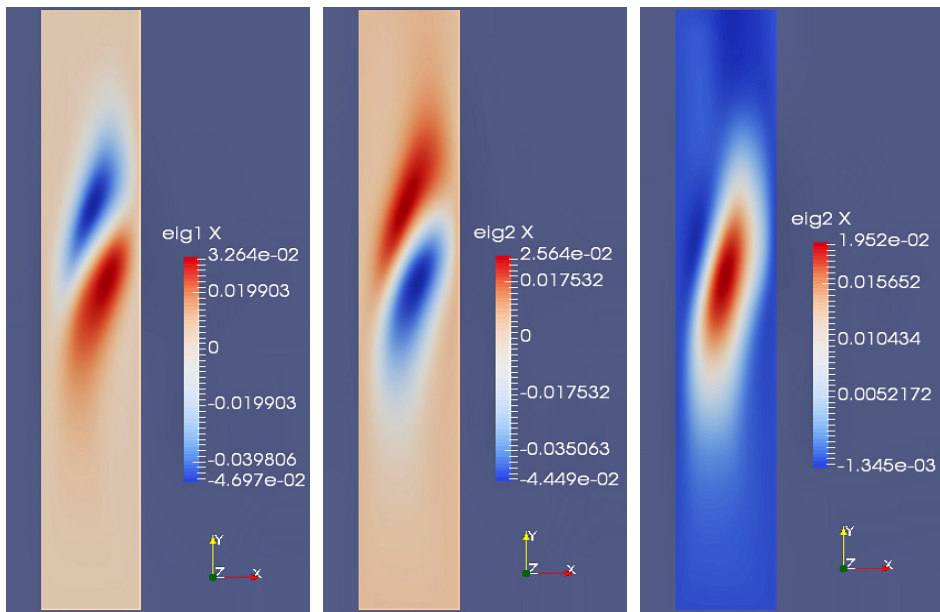

(a) Magnitude of perturbation velocity with $\beta = 4$ (b) Magnitude of perturbation velocity with $\beta = 5$ (c) Magnitude of perturbation velocity with $\beta = 6$
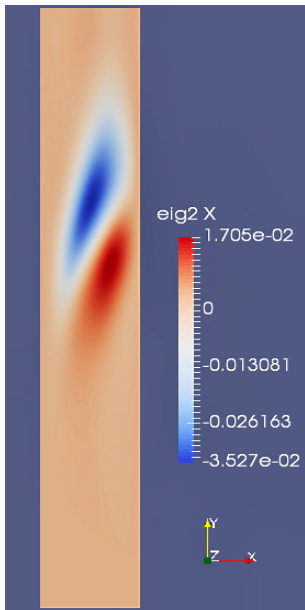
19

(d) Magnitude of perturbation velocity with $\beta = 7$

Figure 16: Magnitude of velocity for the most unstable modes with $\dot{m}/\dot{m}_{design} = 0.73$ and $Re = 890$

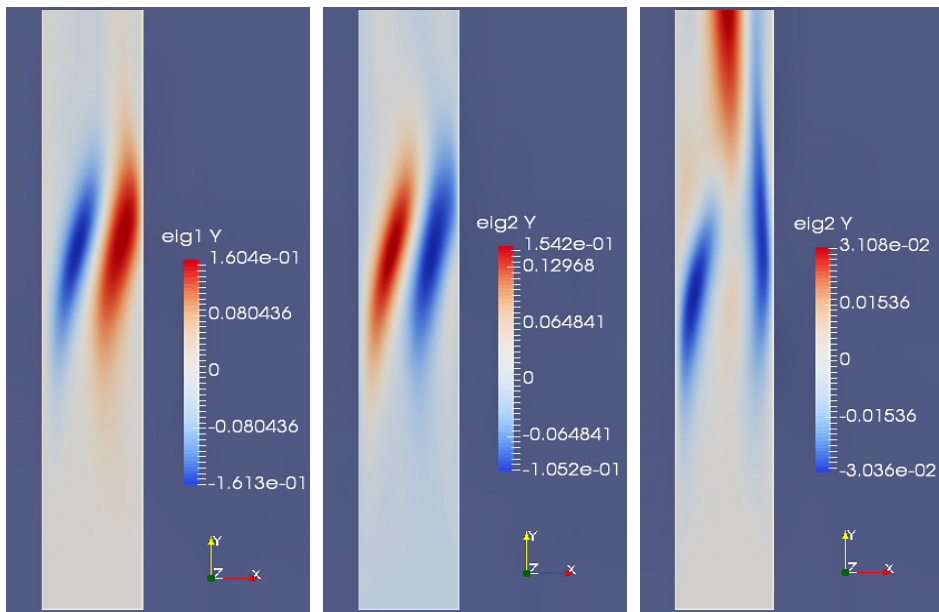(a) Depth component of perturbation velocity with $\beta = 4$

(b) Depth component of perturbation velocity with $\beta = 5$

(c) Depth component of perturbation velocity with $\beta = 6$

20

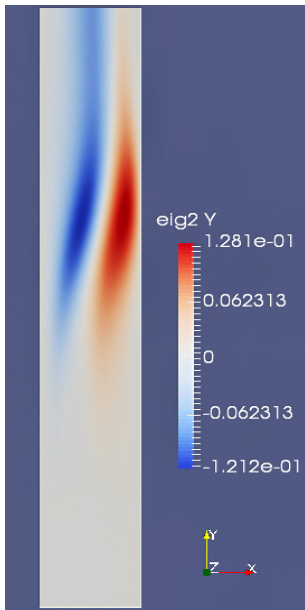(d) Depth component of perturbation velocity with $\beta = 7$

Figure 17: Depth component of velocity for the most instable modes with $\dot{m}/\dot{m}_{design} = 0.73$ and $Re = 890$

(a) Radial component of perturbation velocity with $\beta = 4$
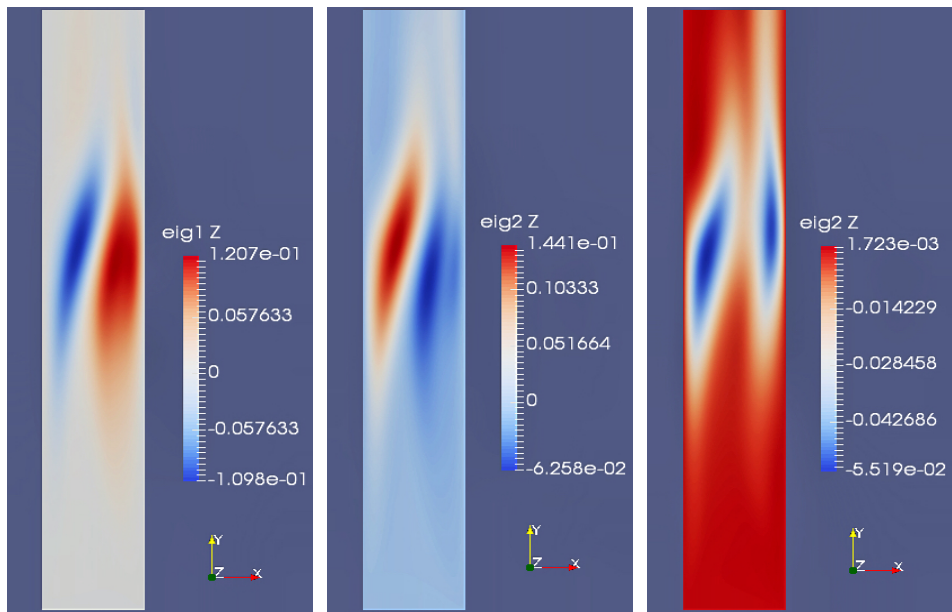
(b) Radial component of perturbation velocity with $\beta = 5$

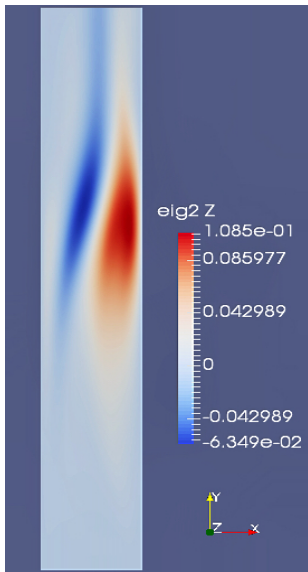(c) Radial component of perturbation velocity with $\beta = 6$

(d) Radial of perturbation velocity with $\beta = 7$

Figure 18: Radial component of velocity for the most unstable modes with $\dot{m}/\dot{m}_{design} = 0.73$ and $Re = 890$
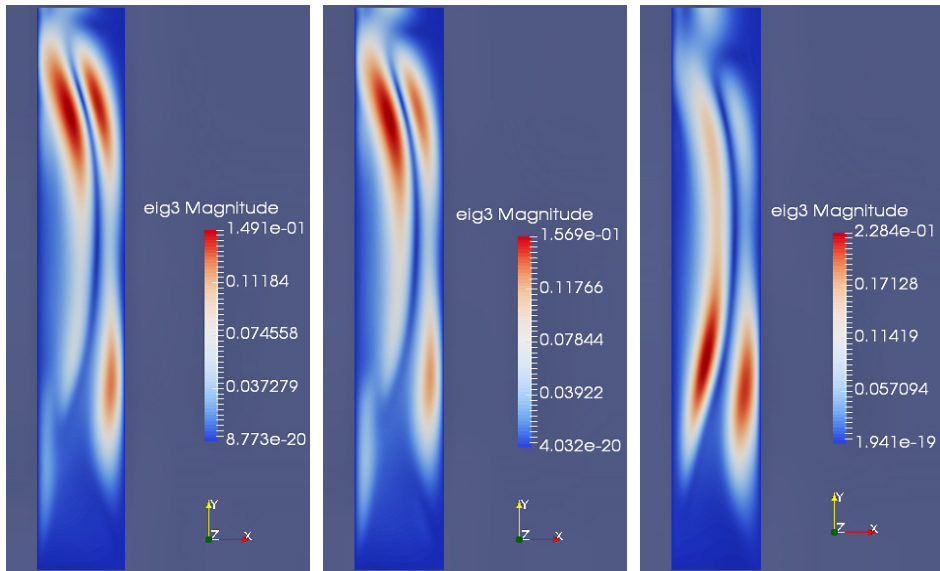

(a) Azimuthal component of perturbation velocity with $\beta = 4$ (b) Azimuthal component of perturbation velocity with $\beta = 5$ (c) Azimuthal component of perturbation velocity with $\beta = 6$

(d) Azimuthal component of perturbation velocity with $\beta = 7$

Figure 19: Azimuthal component of velocity for the most instable modes with $\dot{m}/\dot{m}_{design} = 0.8$ and $Re = 890$
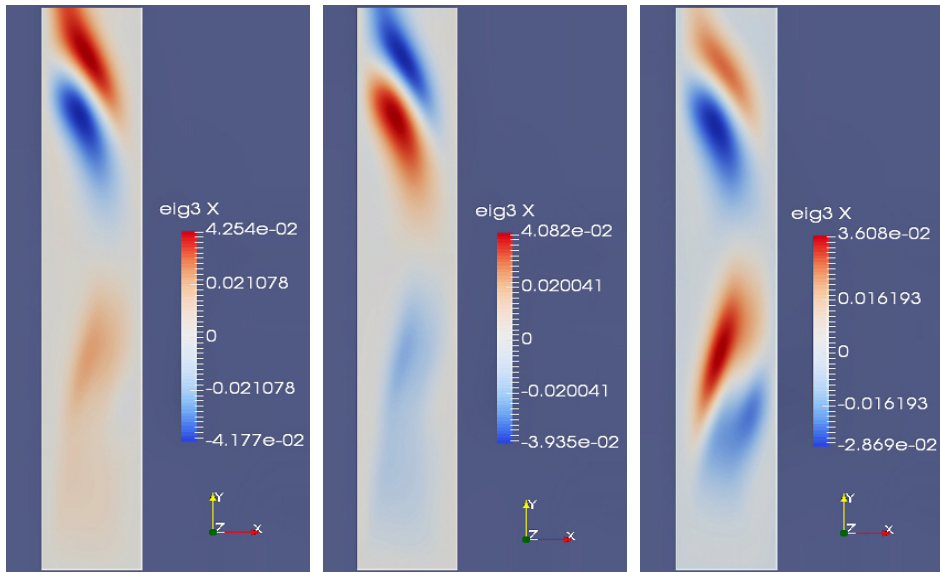

(a) Magnitude of perturbation velocity with $\beta = 5$

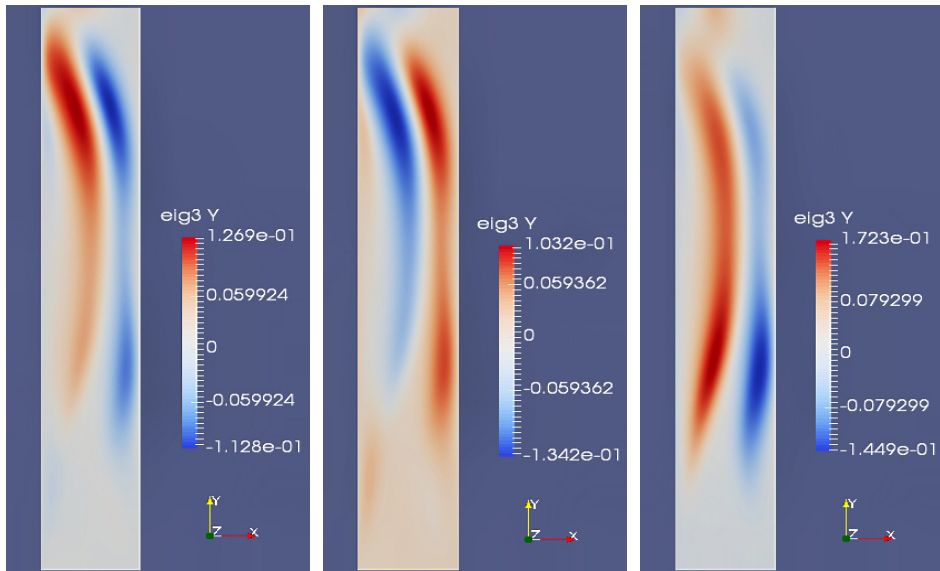(b) Magnitude of perturbation velocity with $\beta = 6$

(c) Magnitude of perturbation velocity with $\beta = 7$

Figure 20: Magnitude of velocity for the most unstable modes for $\dot{m}/\dot{m}_{design} = 0.66$ and $Re = 890$
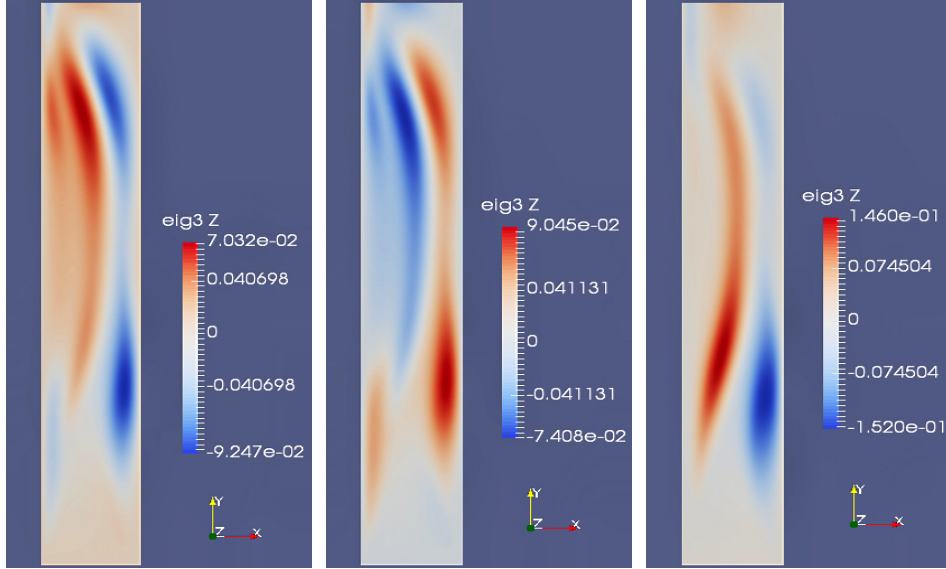
(a) Depth component of pertur- (b) Depth component of pertur- (c) Depth component of pertur-
bation velocity with $\beta = 5$ bation velocity with $\beta = 6$ bation velocity with $\beta = 7$

Figure 21: Depth component of velocity for the most instable modes with $\dot{m}/\dot{m}_{design} = 0.66$ and $Re = 890$

(a) Radial component of pertur- (b) Radial component of pertur- (c) Radial component of pertur-
bation velocity with $\beta = 5$ bation velocity with $\beta = 6$ bation velocity with $\beta = 7$

Figure 22: Radial component of velocity for the most instable modes with $\dot{m}/\dot{m}_{design} = 0.66$ and $Re = 890$

24

(a) Azimuthal component of perturbation velocity with $\beta = 5$ (b) Azimuthal component of perturbation velocity with $\beta = 6$ (c) Azimuthal component of perturbation velocity with $\beta = 7$

Figure 23: Azimuthal component of velocity for the most instable eigenvectors with $\dot{m}/\dot{m}_{design} = 0.66$ and $Re = 890$

6 Sensitivity

The sensitivity properties of the leading global mode are then investigated by computing and making use of the properties of the corresponding adjoint mode, $\hat{v}$, which is solution of the adjoint eigenvalue problem in eq. (6). The parameter ψ displayed in figures (24), (26), (25), has the same definition of s recalled from the equation (7) and represents the structural sensitivity of the flow inside this vaneless diffuser. The red pitch is always located near the left side of the channel but at different radial position from almost the beginning till the half of the total height. In the zones with the highest sensitivity it's possible to introduce a kind of disturbance in the flow field in order to control the instability. The positions of the largest red zones (high sensitivity) are related to the position of the vortex in the perturbed fields described in the previous section except the small zones near the outlet in figures (25), (26) that seem to be a bit unphysical and due to numerical errors with the boundary conditions.
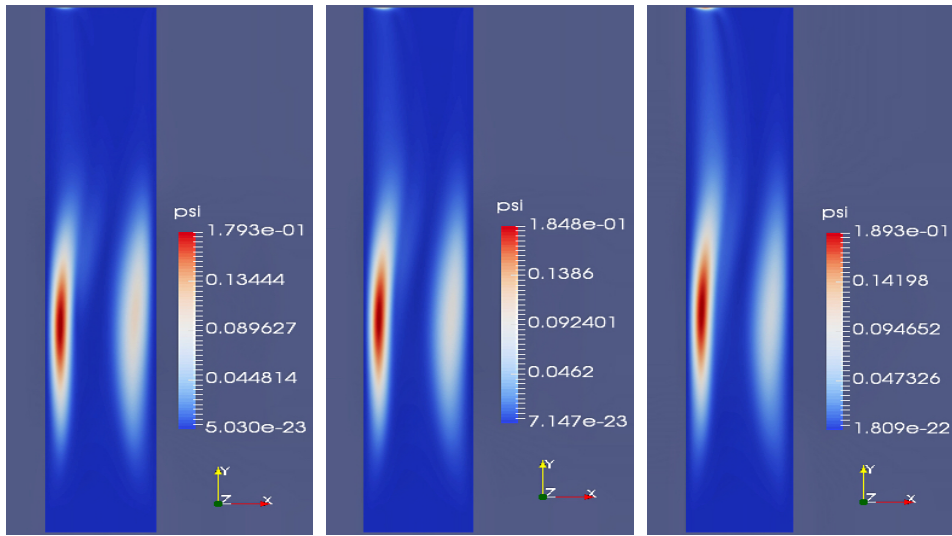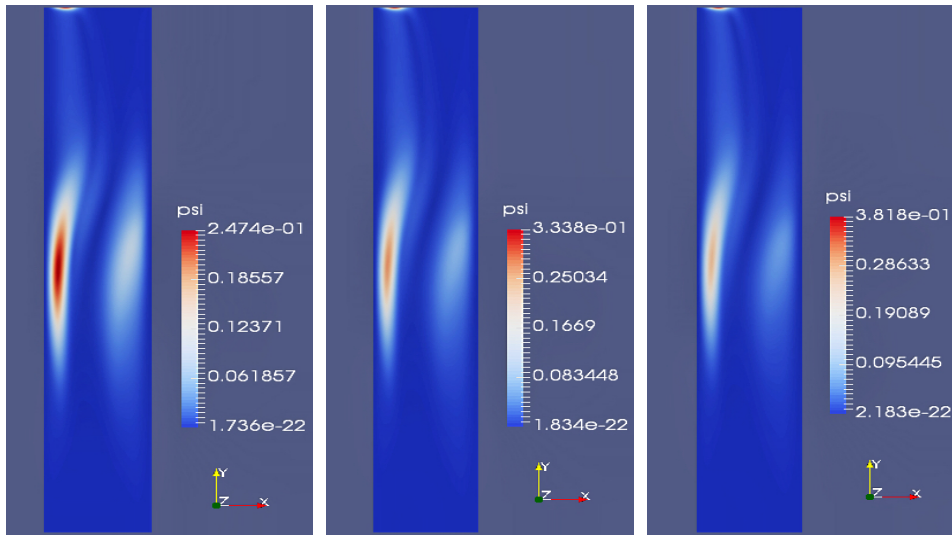
(a) Sensitivity analysis of the unstable global mode with $\beta = 3$

(b) Sensitivity analysis of the unstable global mode with $\beta = 4$

(c) Sensitivity analysis of the unstable global mode with $\beta = 5$
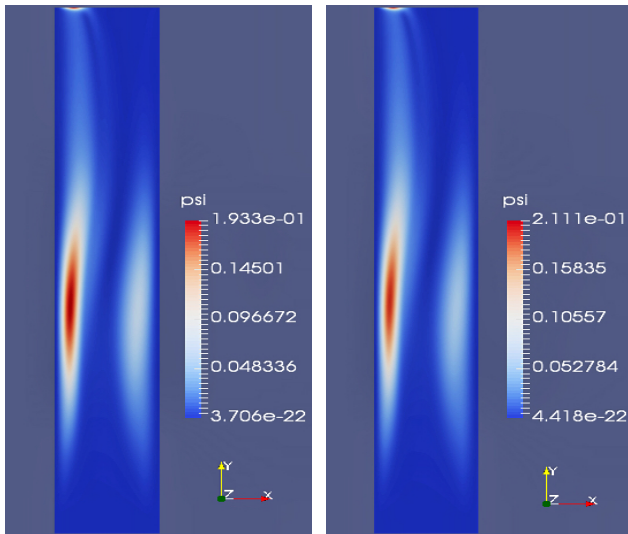
(d) Sensitivity analysis of the unstable global mode with $\beta = 6$

(e) Sensitivity analysis of the unstable global mode with $\beta = 7$

Figure 24: Sensitivity analysis of the unstable global mode with $\dot{m}/\dot{m}_{design} = 0.8$ and $Re = 890$

(a) Sensitivity analysis of the unstable global mode with $\beta = 4$

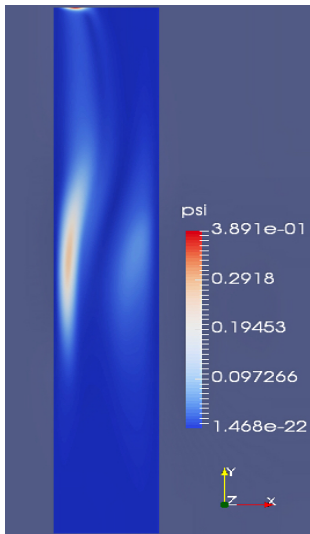(b) Sensitivity analysis of the unstable global mode with $\beta = 5$

(c) Sensitivity analysis of the unstable global mode with $\beta = 6$

(d) Sensitivity analysis of the unstable global mode with $\beta = 7$

Figure 25: Sensitivity analysis of the unstable global mode with $\dot{m}/\dot{m}_{design} = 0.73$ and $Re = 890$
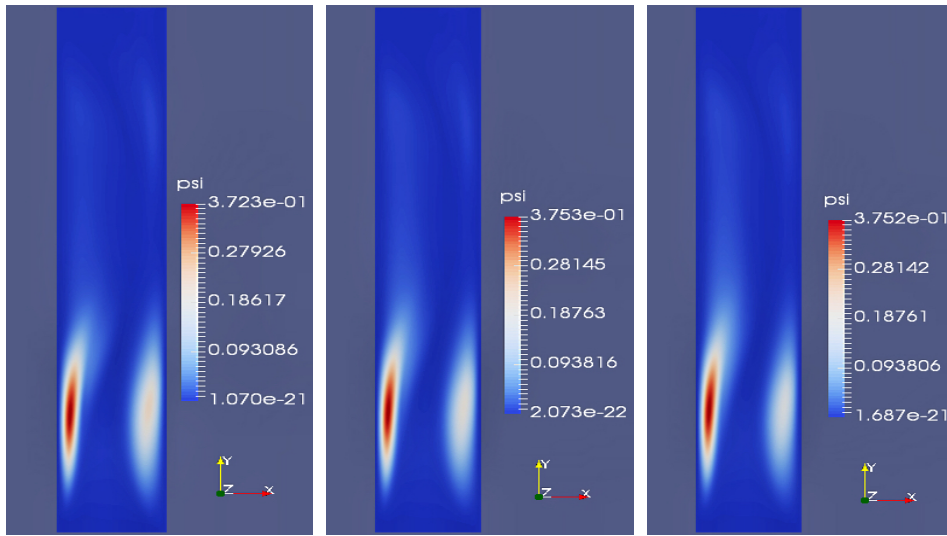
(a) Sensitivity analysis of the unstable global mode with $\beta = 5$ (b) Sensitivity analysis of the unstable global mode with $\beta = 6$ (c) Sensitivity analysis of the unstable global mode with $\beta = 7$

Figure 26: Sensitivity analysis of the unstable global mode with $\dot{m}/\dot{m}_{design} = 0.66$ and $Re = 890$

References

AUTERI, FRANCO 2016 *pastaAxi3d*. Politecnico di Milano, Dipartimento di Ingegneria Aerospaziale.

CANTON, JACOPO 2012-2013 Global linear stability of axisymmetric coaxial jets. PhD thesis, POLITECNICO DI MILANO Facoltà di Ingegneria Industriale Corso di Laurea Magistrale in Ingegneria Aeronautica.

CARINI, M., AIRIAU, C., DEBIEN, A., LÉON, O. & PRALITS, J. O. 2016 Global stability and control of the confined turbulent flow past a thick flat plate. *Physics of Fluids, vol 29, 024102* .

S. LJEVAR, H. C. DE LANGE, A. A. VAN STEENHOVEN 2006 Two-dimensional rotating stall analysis in a wide vaneless diffuser. *International Journal of Rotating Machinery, vol. 2006, 1-11* .

SIPP, DENIS & LEBEDEV, ANTON 2007 Global stability of base and mean flows: a general approach and its applications to cylinder and open cavity flows. *Journal Of Fluid Mechanics, vol. 593, 333–358* .